Editors' Suggestion

Site- and spin-dependent coupling at the highly ordered *h*-BN/Co(0001) interface

Dmitry Yu. Usachov,[1,*] Artem V. Tarasov,[1] Kirill A. Bokai,[1] Viktor O. Shevelev,[1] Oleg Yu. Vilkov,[1] Anatoly E. Petukhov,[1] Artem G. Rybkin,[1] Ilya I. Ogorodnikov,[2] Mikhail V. Kuznetsov,[2] Matthias Muntwiler,[3] Fumihiko Matsui,[4] Lada V. Yashina,[5] Clemens Laubschat,[6] and Denis V. Vyalikh[7,8]

[1]*St. Petersburg State University, 7/9 Universitetskaya nab., St. Petersburg, 199034, Russia*
[2]*Institute of Solid State Chemistry of the Ural Branch of the Russian Academy of Sciences, Pervomayskaya Str. 91, 620990 Ekaterinburg, Russia*
[3]*Paul Scherrer Institut, Villigen, Switzerland*
[4]*Institute for Molecular Science, Myodaiji, Okazaki, 444-8585, Japan*
[5]*M.V. Lomonosov Moscow State University, Leninskie Gory 1/3, 199991 Moscow, Russia*
[6]*Institute of Solid State and Materials Physics, Technische Universität Dresden, 01062 Dresden, Germany*
[7]*Departamento de Fisica de Materiales and CFM-MPC UPV/EHU, Donostia International Physics Center (DIPC), 20080 San Sebastian, Spain*
[8]*IKERBASQUE, Basque Foundation for Science, 48011 Bilbao, Spain*

(Received 14 August 2018; revised manuscript received 15 October 2018; published 26 November 2018)

Using photoelectron diffraction and spectroscopy, we explore the structural and electronic properties of the hexagonal boron nitride (*h*-BN) monolayer epitaxially grown on the Co(0001) surface. Perfect matching of the lattice parameters allows formation of a well-defined interface where the B atoms occupy the hollow sites while the N atoms are located above the Co atoms. The corrugation of the *h*-BN monolayer and its distance from the substrate were determined by means of R-factor analysis. The obtained results are in perfect agreement with the density functional theory (DFT) predictions. The electronic structure of the interface is characterized by a significant mixing of the *h*-BN and Co states. Such hybridized states appear in the *h*-BN band gap. This allows to obtain atomically resolved scanning tunneling microscopy (STM) images from the formally insulating 2D material being in contact with ferromagnetic metal. The STM images reveal mainly the nitrogen sublattice due to a dominating contribution of nitrogen orbitals to the electronic states at the Fermi level. We believe that the high quality, well-defined structure and interesting electronic properties make the *h*-BN/Co(0001) interface suitable for spintronic applications.

DOI: 10.1103/PhysRevB.98.195438

I. INTRODUCTION

It has been a decade since two-dimensional (2D) materials showed up at the forefront of research [1]. Rapidly they became undeniable leaders for applications in future electronics, spintronics, catalysis, energy storage, etc. [2]. Among the wide diversity of 2D materials, the hexagonal boron nitride (*h*-BN) monolayer is one of the most prominent objects. Being isostructural to graphene, this material, in contrast, exhibits insulating properties and presents an atomically thin wide band gap 2D crystal [3,4]. Due to its chemical inertness, a *h*-BN surface of high structural perfection serves as an ideal substrate for epitaxial graphene and other 2D materials [5–7]. Combining graphene and *h*-BN in heterostructures enables a much broader range of their applications and holds out a hope to substitute silicon in electronic devices [8,9]. Moreover, it has been shown that *h*-BN may be successfully used as a tunnel barrier between ferromagnetic contacts and graphene, enabling efficient injection of spin-polarized current in graphene for spintronic applications [10–12].

Device applications require a controllable way of producing large-area *h*-BN layers of high quality. Similarly to graphene, the most suitable preparation method is chemical vapor deposition (CVD). By means of CVD, one or few layers of *h*-BN can be grown on various metal substrates using different precursors, with borazine ($B_3N_3H_6$) being the most popular compound among them [13,14]. Depending on the substrate underneath, the *h*-BN monolayer can form either a planar or a corrugated film. In the particular case of Ni(111) substrate, a commensurate (1×1) structure is formed due to matching of lattice periods [15–25]. Growth on the lattice-mismatched surfaces like on Ni (100) and (110) faces [26,27], Pt(111) [15,28], Pd(111) [29], Cu(111) [16,30], Ir(111) [31,32], Rh(111) [33], Ru(0001) [34], and Fe(110) [35] gives rise to a moire structure. In the case of the strong interaction between a *h*-BN monolayer and its substrate, a rather strongly corrugated nanomesh can be formed [36].

Although the *h*-BN monolayer grown on various transition metal surfaces is well-studied, the *h*-BN/Co interface remains rather unexplored. Cobalt attracts particular attention because of its strong magnetic moment enabling the implementation of spin-valve heterostructures [11,12,37] based on the *h*-BN/Co contacts. Theory predicts enhanced tunneling magnetoresistance in a Co(0001)/*h*-BN/Co(0001) magnetic tunnel junction

*dmitry.usachov@spbu.ru

[38]. Furthermore, the Co(0001) surface possesses a low lattice mismatch with respect to *h*-BN. This may allow formation of an epitaxial (1×1) interface with high structural perfection, similarly to the recently studied graphene/Co(0001) interface [39]. Indeed, several works reported formation of *h*-BN films of different thickness on the Co(0001) surface and confirmed strict orientation of ultrathin *h*-BN [40–42]. However, the crystal structure of the *h*-BN monolayer on the Co(0001) surface is yet to be studied.

This work is aimed at a comprehensive investigation of the interface geometry and the electronic band structure of a monolayer *h*-BN epitaxially grown on a Co(0001) surface by means of CVD using borazine as a precursor. We use x-ray photoelectron spectroscopy (XPS), low energy electron diffraction (LEED), photoelectron diffraction (PED), and scanning tunneling microscopy (STM) to characterize the atomic structure of the *h*-BN/Co(0001) system. Angle resolved photoelectron spectroscopy (ARPES) supported by density functional theory (DFT) calculations provide insight into the interaction of *h*-BN with its substrate and dispersion of electronic states. Our results demonstrate high quality of this ferromagnet-insulator interface and promote its further use in various applications.

II. METHODS

Single-layer *h*-BN was synthesized under the UHV conditions by CVD on a crystalline 15 nm thick Co(0001) film deposited on a clean W(110) surface. The base pressure in the UHV chamber was 5×10^{-10} mbar. The LEED pattern of the Co(0001) film showed a sharp (1×1) hexagonal pattern, indicating high crystallinity of the metal film. The synthesis was carried out as follows: the substrate was heated up to 730 °C then borazine ($B_3N_3H_6$) with a pressure of 3×10^{-7} mbar was introduced into the vacuum chamber for 15 min. Under these conditions, *h*-BN starts to grow immediately on the hot metal surface, and the reaction is self-limited to a single layer. After one monolayer is formed, the growth is terminated as the catalytically active metal surface is passivated with *h*-BN.

The STM and ARPES measurements were performed at the Resource Center "Physical Methods of Surface Investigation" (RC PMSI) of the Research Park of Saint Petersburg State University. The STM data were obtained at the room temperature using the Omicron VT SPM microscope.

The DFT calculations were carried out within the generalized gradient approximation (GGA) to the exchange-correlation potential in the Perdew-Burke-Ernzerhof version [43] as implemented in the FPLO-14.00-48 code (improved version of the original FPLO code by K. Koepernik and H. Eschrig [44]). The system was modeled using a 16-layer-thick Co film with the *h*-BN monolayers on both sides. The atomic positions were relaxed until the forces on each atom were less than 10^{-2} eV/Å. A *k*-point grid of $24 \times 24 \times 1$ was used to sample the Brillouin zone (BZ).

PED data were acquired at room temperature at the PEARL (X03DA) beamline [45] of the Swiss Light Source synchrotron facility using linear polarization of photons. The normal to the sample surface, the x-ray beam, the polarization vector of photons, and the axis of the analyzer lens were oriented in the horizontal plane, while the entrance slit of the Scienta EW4000 electron analyzer was oriented vertically. PED maps were measured by rotating the sample with a polar angle step of 1° and azimuthal angle step of 15°, while the acceptance angle of the analyzer was restricted to ±18°. The 2D electron detector allowed mapping of the angular distribution with an azimuthal angle step of less than 0.5°.

Prior to analysis, the measured photoemission intensity $I(\theta, \phi)$ was normalized to take into account the varying area of the x-ray beam spot on the sample surface during measurements according to the relation $I^e(\theta, \phi) = I(\theta, \phi) \cos(\beta - \theta)$, where $\beta = 60°$ is the angle between the beam and the analyzer, θ is a polar angle, and ϕ is an azimuthal angle. Afterwards, the PED data were projected. Although the most popular projection is stereographic, here, we used an equal-area projection $I^e(r, \phi) = I^e(\theta, \phi)$, which is defined by the relation $r^2 = 1 - \cos\theta$. In this projection, the area of any projected PED feature is proportional to the corresponding solid angle of photoemission.

Simulations of PED were performed using the multiple electron scattering (MS) approximation within the cluster-model approach as implemented in the EDAC code [46]. For quantitative comparison of the calculated and measured PED maps, we have used a reliability factor (*R* factor). The optimal structure corresponds to the minimum of the *R* factor, which was used in the following form:

$$R(\vec{\alpha}) = \sum_{p=1}^{n} \omega_p R_p(\vec{\alpha}), \tag{1}$$

where n is the number of analyzed PED images (in our case $n = 2$), ω_p is a weight factor (we chose $\omega_1 = \omega_2 = 0.5$), $\vec{\alpha}$ is the vector of structural and nonstructural parameters of simulation, and $R_p(\vec{\alpha})$ is the *R* factor of each PED image. The latter is defined in the following way:

$$R_p(\vec{\alpha}) = \frac{1}{N_p} \sum_{i=1}^{N_p} \left(\chi_{pi}^t(\vec{\alpha}) - \chi_{pi}^e\right)^2, \tag{2}$$

where N_p is the number of data points in the corresponding PED image, and χ^t and χ^e are theoretical and experimental PED maps with subtracted background. In particular,

$$\chi_{pi}^* = \frac{I_{pi}^* - I_{0pi}^*}{\sigma_p^*}, \tag{3}$$

where $*$ stands for either experimental (e) or theoretical (t) value, I_{pi}^* is the calculated or measured intensity, I_{0pi}^* is the smooth background intensity, and the value of σ^* is calculated as

$$\sigma_p^* = \sqrt{\frac{1}{N_p} \sum_{i=1}^{N_p} (I_{pi}^* - I_{0pi}^*)^2}. \tag{4}$$

The background I_0^* was determined by a least-squares fitting of the projected intensity $I^*(r, \phi)$ with the smooth function of three parameters chosen as

$$I_0^*(r) = c_1 \cos(\pi r/2) + c_2 \sin^2(\pi r) + c_3 \cos(3\pi r/2). \tag{5}$$

The minimum of the $R(\vec{\alpha})$ was found using the Levenberg-Marquardt algorithm for solving the nonlinear least squares problem. When the optimal parameters $\vec{\alpha}_0$ are found, it is

necessary to estimate their uncertainties. For this purpose we estimate the changes of optimal parameters $\Delta\vec{\alpha}$ caused by the changes of the input data $\Delta\vec{X}$ in a linear approximation, which is supposed to be valid for small $\Delta\vec{X}$:

$$\Delta\vec{\alpha} = (J^T J)^{-1} J^T \Delta\vec{X}. \tag{6}$$

Here, J is a Jacobian matrix constructed from submatrices J_p of each PED image,

$$J = \begin{pmatrix} J_1 \\ J_2 \\ \dots \end{pmatrix}, \quad J_{p,ij} = \sqrt{\frac{\omega_p}{N_p}} \frac{\partial \chi^t_{pi}}{\partial \alpha_j}. \tag{7}$$

$\Delta\vec{X}$ is a vector, consisting of subvectors $\Delta\vec{X}_p$ of each PED image:

$$\Delta\vec{X} = \begin{pmatrix} \Delta\vec{X}_1 \\ \Delta\vec{X}_2 \\ \dots \end{pmatrix}, \quad \Delta X_{p,i} = \sqrt{\frac{\omega_p}{N_p}} \Delta\chi_{p,i}, \tag{8}$$

where $\Delta\chi_{p,i}$ are random differences between the model χ^t_{pi} and the data χ^e_{pi}.

Further, we assumed that all $\Delta\chi_{p,i}$ are random variables possessing normal distributions with equal dispersions $\delta\chi^2_p = R_p(\vec{\alpha}_0)$ within each PED image. Of course, these variables are not independent. Most of them are strongly correlated. The theoretical errors are systematic and related to approximations of the employed physical models. The experimental errors contain both random noise and systematic errors related to imperfect instrument calibrations. In order to provide a realistic estimation of covariance matrix, we assumed that for each PED image the random vector $\Delta\chi_{p,i}$ has a certain number of degrees of freedom, F_p, that is much less than the total number of points N_p in the PED image. Then the covariance matrix can be estimated for the case where the PED image consists of $N_p = F_p$ data points and the variations of their intensities are uncorrelated:

$$V = \sum_{p=1}^{n} \frac{\omega_p R_p(\vec{\alpha}_0)}{F_p} \cdot (J^T J)^{-1} J_p^T J_p (J^T J)^{-1}, \tag{9}$$

In the case of a single PED image, this expression is simplified to

$$V = \frac{R(\vec{\alpha}_0)}{F} \cdot (J^T J)^{-1}. \tag{10}$$

The variances of the parameters are simply the diagonal elements of the covariance matrix:

$$\delta\alpha_j^2 = V_{jj}. \tag{11}$$

It is worth noting that a significant correlation between parameters may occur in some cases. This will lead to increased uncertainties [47]. Such situation can be detected using the correlation matrix

$$C_{ij} = \frac{V_{ij}}{\sqrt{V_{ii} V_{jj}}}. \tag{12}$$

In our study, the absolute values of the correlation coefficients did not exceed 0.6.

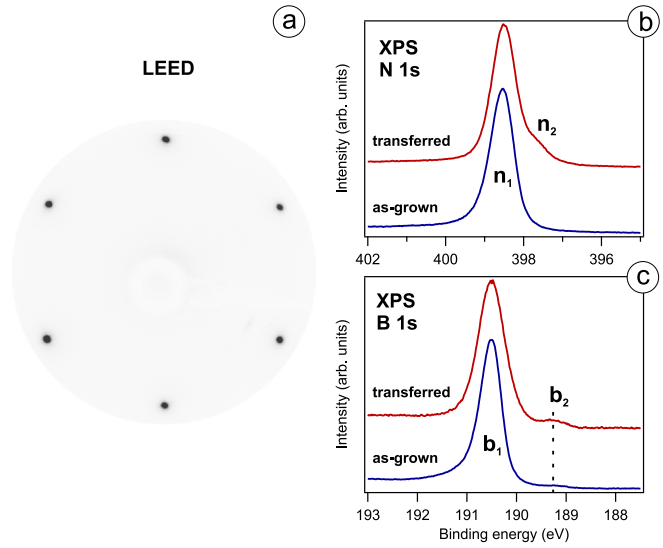

FIG. 1. (a) LEED pattern of the h-BN/Co(0001) system taken at the electron energy of 70 eV. [(b) and (c)] XPS spectra measured using the photon energy of 490 eV.

III. RESULTS AND DISCUSSION

A single-layer h-BN was grown on a single-crystalline Co(0001) film formed on a W(110) substrate as described in the Methods section. Figure 1(a) shows the LEED pattern of the h-BN/Co(0001) system. It exhibits sharp reflexes arranged in a hexagon demonstrating that the h-BN layer is perfectly oriented. The unsplit shape of reflexes indicates that the lattice periods of h-BN and Co(0001) surface are matched within an accuracy better than 0.5%, determined by the width of reflexes. The thickness of the h-BN film was estimated by XPS as 3.3 ± 0.3 Å, which corresponds to a single atomic layer.

Although h-BN is chemically inert at ambient conditions, we have found that the h-BN/Co(0001) interface is highly sensitive to air. Therefore the samples were transferred between different setups in argon atmosphere and further annealed in vacuum at the temperature of $\sim 400\,^{\circ}$C in order to desorb the contaminants. However, this precaution did not completely exclude contact with oxygen and consequent degradation of sample quality. This is illustrated by the XPS spectra shown in Figs. 1(b) and 1(c). The as-grown h-BN layer is characterized with a single peak n_1 in the N 1s XPS spectrum. After transferring in argon and postannealing, a shoulder n_2 appeared at the lower binding energy (BE) side of the N 1s peak. Similar behavior was observed in the C 1s spectra of the graphene/Co(0001) samples exposed to air [48]; these spectral changes were explained by oxygen intercalation underneath graphene. We suppose that in the case of h-BN/Co(0001) system a similar process occurs partially, i.e., at some places on the surface. The B 1s spectrum of the as-grown h-BN layer demonstrates a single peak b_1 with a tiny additional component b_2, indicating presence of some defects in h-BN. The concentration of B atoms related to these defects is about 2 at.% as it was estimated from the b_2/b_1 intensity ratio. After transferring, the number of defects is notably increased as it is evidenced by the higher intensity of the b_2 peak. Nevertheless,

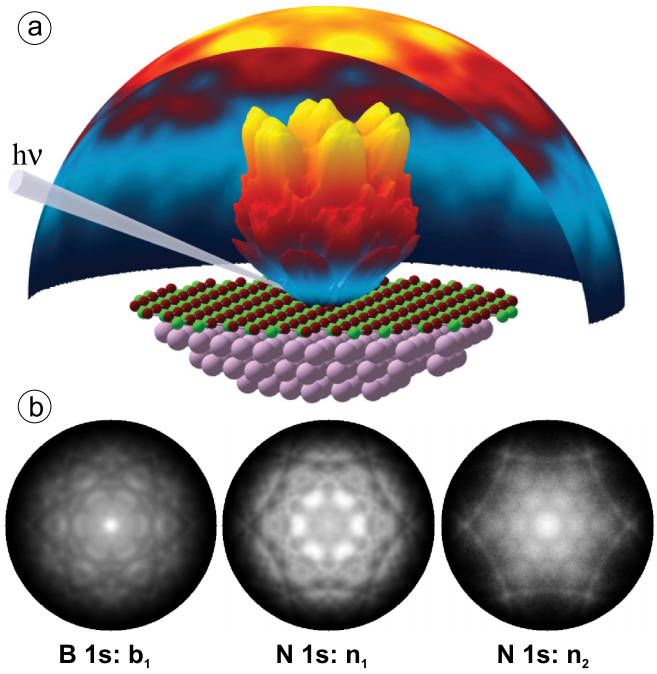

FIG. 2. (a) Scheme of the PED experiment and the *h*-BN/Co(0001) cluster used for the PED simulations. (b) Measured PED intensities in equal area projection.

the main n_1 and b_1 peaks remained almost unchanged, which allowed us to perform structural studies at distant synchrotron radiation facility.

To gain a deep insight into the structure of the *h*-BN/Co(0001) interface we carried out PED measurements of the B 1*s* and N 1*s* core levels in angular mode. This technique was successfully applied to study the structure of 2D materials including *h*-BN monolayer [32,49]. To ensure high sensitivity of PED data to the position of the *h*-BN layer with respect to the substrate, we used a relatively low photoelectron kinetic energy of 300 eV, at which photoelectron backscattering has a notable contribution to the PED pattern. The measured angular distribution of the n_1 peak intensity is illustrated in Fig. 2(a). The normalized and projected intensities are shown in Fig. 2(b). The n_1 and b_1 peaks demonstrate sharp PED patterns indicating good crystallinity of the corresponding *h*-BN surface. In contrast, the n_2 peak exhibits a rather unsharp pattern, although it demonstrates some similarity to the n_1 pattern. This means that the N atoms related to the peak n_2 still belong to *h*-BN, but they do not have well-defined position relative to the substrate. This is consistent with the assumption on the oxygen intercalation underneath some parts of the *h*-BN layer. Therefore we focused at the analysis of the n_1 and b_1 patterns, ascribed to the intact interface.

The measured n_1 and b_1 intensities after background subtraction are shown in Fig. 3(a). In order to determine the structure of the interface, it is necessary to find the atomic

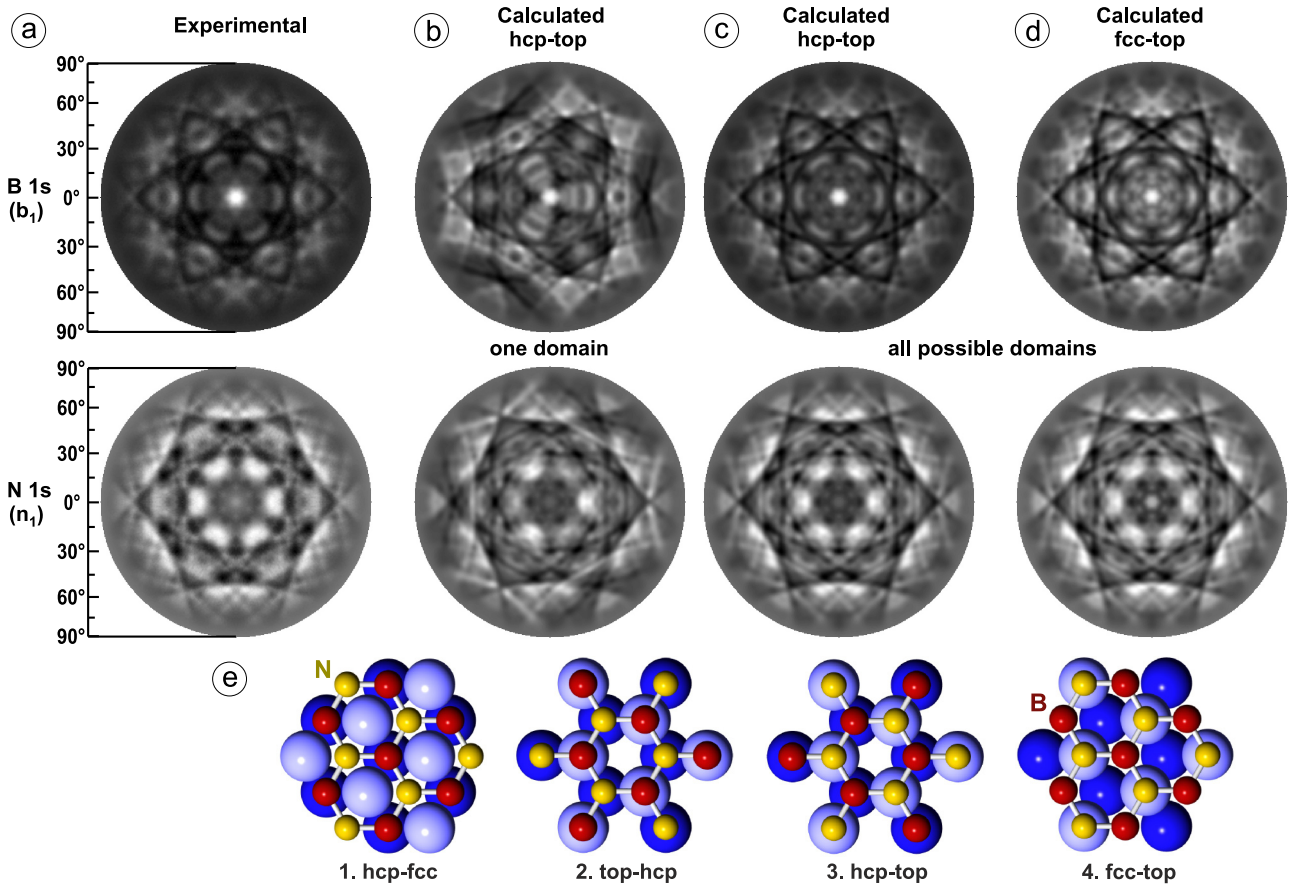

FIG. 3. (a) Experimental and (b)–(d) calculated PED images of *h*-BN/Co(0001) system in the equal area projection. (e) Several structures of the interface and their notations.

arrangement that gives the global minimum of the R factor. For this purpose we considered different positions of the h-BN layer relative to the cobalt surface. Several high-symmetry positions are illustrated in Fig. 3(e). Our DFT calculations, which will be discussed further, showed that among these positions the hcp-top and fcc-top structures are most favorable energetically. Therefore these structures were chosen as starting points for the PED analysis.

In order to calculate a PED image for a given lateral position of the h-BN layer, we considered the R factor as a function of two structural parameters, namely B-Co and N-Co interlayer distances, and unknown nonstructural parameters, such as inner potential, Debye temperature, and the height of the interface between solid and vacuum. Then the minimum of the R factor was found. The calculated PED images at optimal parameters determined for the hcp-top and fcc-top structures are shown in Figs. 3(c) and 3(d). They are rather similar to each other because in both structures the N atoms occupy positions atop the Co atoms and the B atoms are located above the hollow sites. All simulated images demonstrate good agreement with experimental data, however, the hcp-top structure fits slightly better.

It should be noted that because of the ABAB stacking of Co atomic layers, there are two possible surface terminations (A and B). Therefore there are two possible orientations of the h-BN layer. Thus the interface should consist of at least two types of domains. Figure 3(b) shows the PED images calculated for one orientation. Obviously, it has threefold symmetry. However, the experimental data exhibit sixfold symmetry, indicating that the PED pattern is formed by the sum of PE signals from different domains.

In order to consider all possible positions of the h-BN monolayer, we have calculated the dependence of R factor on the lateral displacement of h-BN. In each step, we have optimized the structural and nonstructural parameters to minimize the R factor. The results are presented in Fig. 4. The numbers on the R-factor maps indicate the corresponding structures shown in Fig. 3(e). The global minimum was achieved for the hcp-top structure (position 3), which has R = 0.22. The second deep minimum corresponds to the fcc-top configuration (position 4) with R = 0.25. The other local minimum is observed for the hcp-fcc structure (position 1) with R = 0.37.

To determine the significance of the R-factor minimum, it is useful to estimate its variance. If we assume that the deviations between the calculated and measured PE intensities are random variables possessing normal distributions with identical variances, then each R_p obeys a chi-squared distribution, and the standard deviation of the R factor can be found as

$$\delta R = \sqrt{2\sum_{p=1}^{n} \frac{\omega_p^2}{F_p} R_p^2(\vec{\alpha}_0)}, \tag{13}$$

Where F_p is a number of statistical degrees of freedom for a given PED pattern. In the case of single PED image, this expression turns to the formula $\delta R/R = \sqrt{2/F}$ suggested by Pendry [50]. The F value can be considered as the number of independent pieces of structural information contained in the data [47]. This number can hardly be determined reliably. One straightforward approach is to relate F to the number

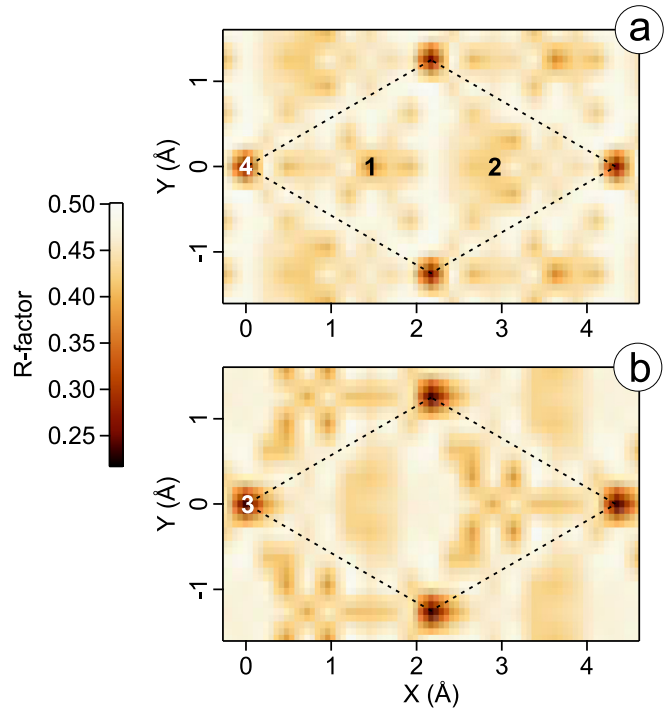

FIG. 4. Calculated dependence of R factor on the lateral shift of the h-BN layer relative to (a) the fcc-top position, (b) the hcp-top position. Dashed line shows the unit cell.

of characteristic features in the PED data. All PED images consist of a set of features like intensity maxima or minima. In the calculated images, these features differ in position and intensity with respect to the experimental data. Thus the deviations between theoretical and experimental intensities are strongly correlated for neighboring photoemission directions in the vicinity of each feature. This fact lets us suppose that the number of degrees of freedom can be approximated by the number of features. In order to determine the number of features automatically, we used an autocorrelation function of the experimental PED projection $\chi_p^e(x, y)$:

$$f_p(x', y') = \iint \chi_p^e(x, y)\chi_p^e(x - x', y - y')dxdy. \tag{14}$$

The number of features F_p can be roughly estimated as the total area of PED image A_p divided by the cross-section area a_p of the central peak in $f_p(x', y')$ at the level of 39.1% of its height. This threshold value is chosen in analogy with the case of ideal circular feature, the size of which is equal to the cross section of the autocorrelation function at this particular level. Moreover, if the PED map contains symmetry elements, the F_p value should be divided by the symmetry order S to exclude counting of identical features. Hence we have $F_p = A_p/(a_p S)$. In the case of BN/Co(0001) system, the symmetry order is $S = 12$ because of a sixfold axis and a mirror plane. The estimated numbers of independent features are $F_{B1s} = 13$ and $F_{N1s} = 19$. These numbers roughly correspond to the numbers of features counted by eye. Of course, the validity of this approach requires further justifications.

In frames of assumptions discussed above, for the hcp-top structure, we obtain $\delta R = 0.06$. This value exceeds the

TABLE I. Optimal parameters determined with EDAC: $d_{\text{N-B}}$ is the height difference between the N and B atomic layers, $d_{\text{B-Co}}$ is the distance between the B layer and the Co surface, and V_0 is the inner potential. B atoms are closer to Co than N atoms.

	hcp-top	fcc-top
$d_{\text{N-B}}$, Å	0.07 ± 0.02	0.06 ± 0.02
$d_{\text{B-Co}}$, Å	2.04 ± 0.02	2.03 ± 0.02
V_0, eV	19 ± 2	20 ± 2

difference between the R factors of the hcp-top and fcc-top structures, which equals to 0.03. Therefore we cannot reliably distinguish these two configurations using the R-factor analysis. This is why we conclude that the h-BN/Co(0001) interface is formed by either hcp-top or fcc-top structures or by the mixture of both.

Let us now focus at the structural parameters determined from the PED analysis. The most important optimal parameters and their uncertainties are presented in Table I. The results demonstrate that the obtained PED data are very sensitive to the interlayer distances. A tiny corrugation of the h-BN layer can be reliably detected. Also, the relative uncertainty of the B-Co interlayer distance is about 1%. It should be noted that even at the most pessimistic estimation of errors obtained by using $F_p = 1$, the relative uncertainty would not exceed 5%.

To determine which structures are more favorable energetically we performed DFT calculations for the four configurations shown in Fig. 3(e). The relative total energies and the optimal structural parameters are given in Table II. It can be seen that the fcc-top structure is the most favorable one. However, the energy of the hcp-top structure differs by only $\Delta E = 5$ meV, which is much less than the energy of thermal vibrations at the temperature of synthesis (and even at the room temperature). The ratio of the probabilities for the formation of the fcc-top and hcp-top structures can be roughly estimated as $\exp(\Delta E / k_B T) = 1.06$, where k_B is the Boltzmann constant and T is the synthesis temperature. For this reason, both fcc-top and hcp-top structures must be formed with rather similar probabilities of 51% and 49%, respectively. Formation of the other configurations like hcp-fcc and top-hcp is highly unfavorable. Comparison of the interlayer distances determined for the fcc-top (or hcp-top) structures by DFT and from PED analysis reveals perfect agreement for the B-Co spacing. However, DFT predicts slightly larger corrugation $d_{\text{N-B}} = 0.13$ Å with respect to the experimental value of 0.07 ± 0.02 Å.

TABLE II. Characteristics of different h-BN/Co(0001) structures determined with DFT: $d_{\text{N-B}}$ and $d_{\text{B-Co}}$ have the same meaning as in Table I, d_{12} is the spacing between the topmost Co layers (note that the calculated interlayer spacing in the bulk is 2.025 Å), ΔE is the total energy per unit cell relative to the fcc-top structure.

	hcp-top	fcc-top	hcp-fcc	top-hcp
$d_{\text{N-B}}$, Å	0.131	0.131	0.021	0.018
$d_{\text{B-Co}}$, Å	2.035	2.036	3.18	3.20
d_{12}, Å	1.947	1.949	1.956	1.956
ΔE, meV	5	0	281	346

It is worth noting that there is a certain structural similarity between the h-BN/Co(0001) system and the well-studied h-BN/Ni(111) system. Both interfaces possess matching of the lattice constants of h-BN and metal. Moreover, in both systems, nitrogen is located in the top position, while boron occupies the hollow sites [15–25]. DFT calculations for the h-BN/Ni(111) system predict the energy difference of 14 meV between the fcc and hcp positions of the B atoms with the fcc position being more favorable [22]. This leads to the probability for the fcc-top structure formation of nearly 54% if the other factors are ignored. However, experimental LEED and PED studies indicate that the fcc-top structure may strongly dominate [23–25], as it is evidenced by the pronounced threefold symmetry of the nearest-neighbor forward scattering pattern in the B 1s PED image [24]. This contradiction indicates strong influence of the kinetic factors and/or surface defects on the h-BN growth on the Ni(111) surface. A newly purchased Ni crystal may have insufficient surface quality for the preferential growth of the fcc-top structure; in this case, a mixture of two configurations can be formed, resulting in a sixfold symmetry of the PED image [45]. In the case of Co(0001) substrate with the ABAB stacking sequence, the presence of AB and BA crystal terminations leads to the two opposite orientations of h-BN. As a result, the PED image has a sixfold symmetry for any type of structure. Therefore discrimination between the fcc-top and hcp-top structures with PED or LEED is much more difficult on the Co(0001) surface than on the Ni(111) single crystal. It should be noted that according to our simulations the enhancement of electron backscattering upon decreasing of the kinetic energy to 80 eV does not provide any improvement in distinguishing between the fcc and hcp boron positions. We suppose that ion scattering spectroscopy may help to identify the structure more precisely [51].

Let us turn to the electronic structure of the h-BN/Co(0001). Figure 5(a) shows the ARPES map measured from the freshly prepared sample. It reveals dispersions of electronic states with the surface sensitivity of a few angstroms. As expected, the data demonstrate π and σ bands of h-BN. Also Co 3d states, located close to the Fermi level, are visible due to monoatomic thickness of the h-BN layer.

The influence of cobalt substrate on the band structure of h-BN can be understood with the help of the DFT results for the h-BN/Co(0001) against a freestanding h-BN monolayer. We have found that the differences between the band structures of the fcc-top and hcp-top structures are negligible, hereat only the bands for the fcc-top configuration are exhibited in Fig. 5(b). One can see the notable energy difference between the π bands of bonded and freestanding h-BN. Such energy shift of the π states of h-BN/Co(0001) is a consequence of their strong hybridization with the Co 3d states.

It should be noted that ferromagnetism of cobalt leads to an exchange splitting of the electronic states. Our calculation predicts a significant spin splitting of the π band near the **K** point of the surface BZ. However, this splitting is not observed in our spin-integrated ARPES data. This can be explained by the fact that at the **K** point the majority π band reaches the energy region of the projected majority Co states, where they become strongly mixed. As a consequence, the contribution of the BN p_z orbitals to the majority wave functions at the **K**

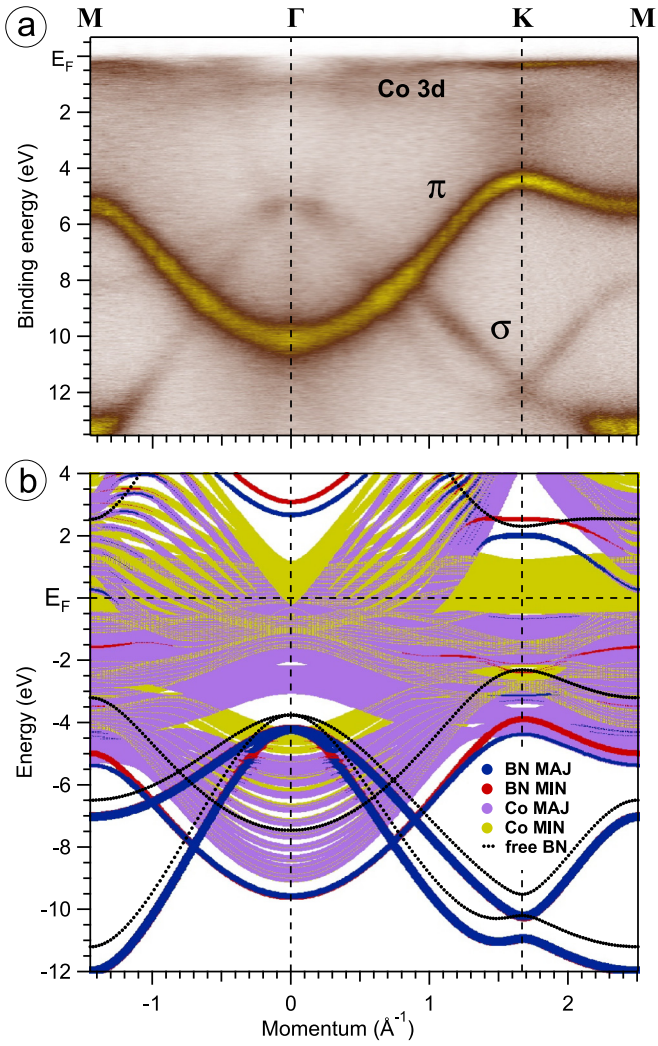

FIG. 5. (a) ARPES map of h-BN/Co(0001) obtained using He II radiation (40.8 eV). (b) Calculated band structures of the *h*-BN/Co(0001) system and the freestanding *h*-BN monolayer. The labels MAJ and MIN denote majority and minority spin directions.

point becomes smeared out over the wide energy range of the Co 3*d* states and does not produce a sharp band in the PE map. The minority π band appears in the projected local band gap of Co, therefore, it is less hybridized and gives a pronounced PE peak observed at the **K** point in experiment.

Although the isolated *h*-BN monolayer is an insulator, it loses its insulating properties on the Co(0001) surface. Due to mixing of the electronic states of *h*-BN and Co, new hybridized states are formed at the Fermi level. This is illustrated in Fig. 6, where the contributions of the B and N orbitals to the electronic states at the Fermi level are shown. It can be seen that the B and N contributions to the minority spin states are smeared over the surface BZ. The majority spin states form a local band gap around the **K** point. Outside this gap, the N orbitals are mixed with the bulk majority Co states, which are quantized in the direction perpendicular to the surface because of the finite thickness of Co film. The main contribution of the B orbitals to the majority states appears at the border of the local band gap. These states are localized at the surface in contrast to hybridized N-Co majority states.

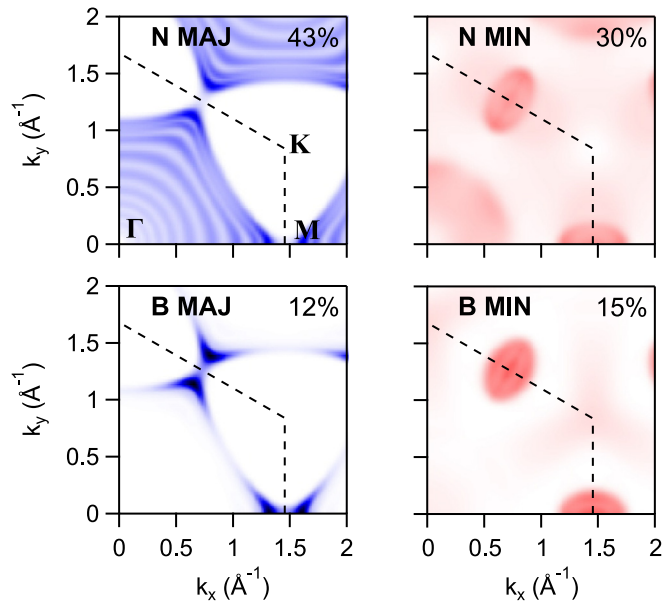

FIG. 6. Calculated momentum-resolved contributions of B and N orbitals to the Fermi surface of the *h*-BN/Co(0001) system. Dashed lines show the surface BZ. The numbers in the right upper corners represent the relative contributions integrated over the whole BZ.

Metallic character of a chemisorbed *h*-BN monolayer allows efficient use of scanning tunneling microscopy (STM) to study the topography and defects of the *h*-BN/Co(0001) interface. Figure 7(a) shows the STM image of the 200-nm wide region of the sample studied immediately after the synthesis. The surface consists of flat terraces and steps of different height. The profile shown in Fig. 7(b) exhibits single atomic steps with the height of 2.0 Å, which corresponds to the interlayer distance in a Co lattice, and a double step. Also, triple steps can be observed in other places. In the upper part of the image, one can see a screw dislocation, which is a rather frequent defect of the cobalt film on the W(110) substrate, according to our data.

Figure 7(b) demonstrates an atomically resolved STM image. It exhibits a periodic hexagonal lattice with the period of 2.5 Å, which is expected for the (1×1) structure of the *h*-BN/Co(0001) interface. However, it does not reveal the honeycomb structure of *h*-BN. This can be explained by the simulated STM image of the fcc-top structure shown in Fig. 7(d). In terms of the Tersoff-Hamann approximation, the tunneling current is proportional to the local density of states (LDOS) at E_F. Our DFT calculation shows that in addition to the slightly higher location of the N atoms relative to the B atoms on the Co(0001) surface, the nitrogen sublattice has notably higher LDOS. This is evidenced by Fig. 6, which shows that 73% of the *h*-BN contribution to the DOS at the Fermi level is provided by the orbitals of nitrogen. This is why the N atoms look higher in the STM image. For the hcp-top structure, the simulated STM image is rather similar, therefore it is not shown. Another prominent feature of the STM image is the presence of several bright spots, which may be related to point defects of either cobalt or *h*-BN. Unfortunately, we could not resolve the structure of these defects and determine their nature.

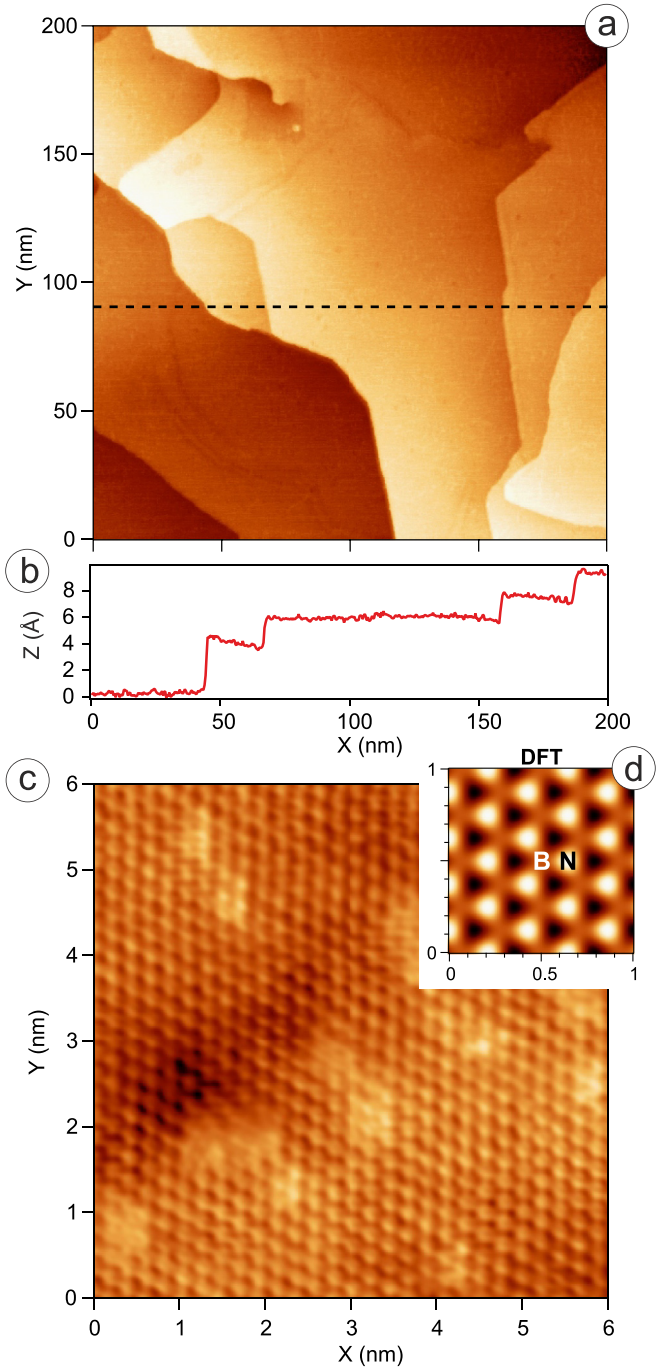

FIG. 7. [(a) and (c)] STM images of the h-BN/Co(0001) surface obtained at a bias voltage $V_t = 200\,\text{mV}$ and a constant current $I_t = 0.3\,\text{nA}$ (a), and at $V_t = 30\,\text{mV}$, $I_t = 1\,\text{nA}$ (c). Light colors correspond to higher regions. Dashed line in (a) corresponds to the image profile (b). (d) Local density of states at the Fermi level calculated by DFT in the energy window of ± 0.1 eV at the height of 2 Å above the surface of the h-BN/Co(0001) system possessing an fcc-top structure.

IV. CONCLUSIONS

In summary, we have demonstrated the formation of a single h-BN layer on the Co(0001) surface. By using ARPES, PED, and STM, we have studied comprehensively the electronic structure and the crystal structure of the interface. Perfect matching of the lattice constants of Co and h-BN results in the formation of an epitaxial (1×1) structure. Comparison of the experimental PED data with the simulated photoemission intensity maps demonstrates that boron atoms preferably occupy hollow sites, while nitrogen atoms are located above Co atoms. Thus the interface is formed by the fcc-top or/and by the hcp-top structures. Although the PED analysis suggests that the hcp-top structure is more favorable than the fcc-top one, we cannot discriminate reliably between these two configurations. According to the DFT calculations, the energy difference between these two structures is negligible, therefore both of them are expected to be formed with similar probabilities during the synthesis.

Despite the fact that h-BN is chemically inert, the h-BN/Co(0001) interface is strongly affected by oxygen. Evidently, oxygen can intercalate the BN layer; however, the mechanism of this process is not yet understood.

The STM images of the h-BN/Co(0001) system demonstrate the high quality of the surface comprised of atomically flat terraces and few-atom-high steps. Atomically resolved images reveal only one of the two h-BN sublattices. This is explained by the DFT simulations of STM images. They show that the nitrogen sublattice exhibits higher local density of states near the Fermi level, therefore it gives a dominating contribution to the tunneling current.

The notable contribution of N and B orbitals to the electronic states at the Fermi level is a consequence of a strong interaction between the h-BN and Co(0001) substrate that is accompanied by a significant hybridization of the BN π and Co $3d$ states. This is evidenced by the ARPES data and supported by the DFT band structure calculations, which confirm formation of hybrid interface states in the energy region of the h-BN band gap. In addition, our calculations predict strong spin splitting of the h-BN π states near the **K** point of the Brillouin zone. One can anticipate that the studied epitaxial h-BN/Co(0001) system will be of interest for applications in electronics and spintronics.

ACKNOWLEDGMENTS

L.V.Ya. acknowledges the RSF (Grant No. 16-42-01093). A.V.T., V.O.S., K.A.B., O.Yu.V., and D.Yu.U. acknowledge St. Petersburg State University for research Grant No. 11.65.42.2017. M.V.K. and I.I.O. acknowledge the RFBR (Grant No. 16-29-06410). C.L. acknowledges the DFG (Grant Nos. LA655-17/1 and LA655-19/1). We thank the Paul Scherrer Institut, Villigen, Switzerland for provision of synchrotron radiation beamtime at beamline PEARL of the SLS.

[1] K. S. Novoselov, A. Mishchenko, A. Carvalho, and A. H. Castro Neto, 2D materials and van der Waals heterostructures, Science **353**, aac9439 (2016).

[2] W. Choi, N. Choudhary, G. Hee Han, J. Park, D. Akinwande, and Y. H. Lee, Recent development of two-dimensional transition metal dichalcogenides

and their applications, Mater. Today **20**, 116 (2017).

[3] G. Giovannetti, P. A. Khomyakov, G. Brocks, P. J. Kelly, and J. van den Brink, Substrate-induced band gap in graphene on hexagonal boron nitride: Ab initio density functional calculations, Phys. Rev. B **76**, 073103 (2007).

[4] L. Song, L. Ci, H. Lu, P. B. Sorokin, C. Jin, J. Ni, A. G. Kvashnin, D. G. Kvashnin, J. Lou, B. I. Yakobson, and P. M. Ajayan, Large scale growth and characterization of atomic hexagonal boron nitride layers, Nano Lett. **10**, 3209 (2010).

[5] C. R. Dean, A. F. Young, I. Meric, C. Lee, L. Wang, S. Sorgenfrei, K. Watanabe, T. Taniguchi, P. Kim, K. L. Shepard, and J. Hone, Boron nitride substrates for high-quality graphene electronics, Nat. Nanotech. **5**, 722 (2010).

[6] M. Zhang, Y. Zhu, X. Wang, Q. Feng, S. Qiao, W. Wen, Y. Chen, M. Cui, J. Zhang, C. Cai, and L. Xie, Controlled synthesis of ZrS_2 monolayer and few layers on hexagonal boron nitride, J. Am. Chem. Soc. **137**, 7051 (2015).

[7] A. Yan, J. Velasco, S. Kahn, K. Watanabe, T. Taniguchi, F. Wang, M. F. Crommie, and A. Zettl, Direct growth of single- and few-layer MoS_2 on h-BN with preferred relative rotation angles, Nano Lett. **15**, 6324 (2015).

[8] A. K. Geim and I. V. Grigorieva, Van der Waals heterostructures, Nature (London) **499**, 419 (2013).

[9] L. Britnell, R. V. Gorbachev, R. Jalil, B. D. Belle, F. Schedin, A. Mishchenko, T. Georgiou, M. I. Katsnelson, L. Eaves, S. V. Morozov, N. M. R. Peres, J. Leist, A. K. Geim, K. S. Novoselov, and L. A. Ponomarenko, Field-effect tunneling transistor based on vertical graphene heterostructures, Science **335**, 947 (2012).

[10] N. Tombros, C. Jozsa, M. Popinciuc, H. T. Jonkman, and B. J. van Wees, Electronic spin transport and spin precession in single graphene layers at room temperature, Nature (London) **448**, 571 (2007).

[11] M. V. Kamalakar, T. I. André Dankert, J. Bergsten, and S. P. Dash, Enhanced tunnel spin injection into graphene using chemical vapor deposited hexagonal boron nitride, Sci. Rep. **4**, 6146 (2014).

[12] M. V. Kamalakar, A. Dankert, P. J. Kelly, and S. P. Dash, Inversion of spin signal and spin filtering in ferromagnet|hexagonal boron nitride-graphene van der Waals heterostructures, Sci. Rep. **6**, 21168 (2016).

[13] A. A. Tonkikh, E. N. Voloshina, P. Werner, H. Blumtritt, B. Senkovskiy, G. Guentherodt, S. S. P. Parkin, and Yu. S. Dedkov, Structural and electronic properties of epitaxial multilayer h-BN on Ni(111) for spintronics applications, Sci. Rep. **6**, 23547 (2016).

[14] Y. Shi, C. Hamsen, X. Jia, K. K. Kim, A. Reina, M. Hofmann, A. L. Hsu, K. Zhang, H. Li, Z.-Y. Juang, M. S. Dresselhaus, L.-J. Li, and J. Kong, Synthesis of few-layer hexagonal boron nitride thin film by chemical vapor deposition, Nano Lett. **10**, 4134 (2010).

[15] A. Nagashima, N. Tejima, Y. Gamou, T. Kawai, and C. Oshima, Electronic Structure of Monolayer Hexagonal Boron Nitride Physisorbed on Metal Surfaces, Phys. Rev. Lett. **75**, 3918 (1995).

[16] A. B. Preobrajenski, A. S. Vinogradov, and N. Mårtensson, Monolayer of h-BN chemisorbed on Cu(111) and Ni(111): The role of the transition metal 3d states, Surf. Sci. **582**, 21 (2005).

[17] A. Nagashima, N. Tejima, Y. Gamou, T. Kawai, and C. Oshima, Electronic dispersion relations of monolayer hexagonal boron nitride formed on the Ni(111) surface, Phys. Rev. B **51**, 4606 (1995).

[18] A. Nagashima, Y. Gamou, M. Terai, M. Wakabayashi, and C. Oshima, Electronic states of the heteroepitaxial double-layer system: Graphite/monolayer hexagonal boron nitride/Ni(111), Phys. Rev. B **54**, 13491 (1996).

[19] A. B. Preobrajenski, A. S. Vinogradov, and N. Mårtensson, Ni $3d$–BN π hybridization at the h-BN/Ni(111) interface observed with core-level spectroscopies, Phys. Rev. B **70**, 165404 (2004).

[20] D. Usachov, V. K. Adamchuk, D. Haberer, A. Grüneis, H. Sachdev, A. B. Preobrajenski, C. Laubschat, and D. V. Vyalikh, Quasifreestanding single-layer hexagonal boron nitride as a substrate for graphene synthesis, Phys. Rev. B **82**, 075415 (2010).

[21] V. M. Karpan, P. A. Khomyakov, G. Giovannetti, A. A. Starikov, and P. J. Kelly, Ni(111)|graphene|h-BN junctions as ideal spin injectors, Phys. Rev. B **84**, 153406 (2011).

[22] G. B. Grad, P. Blaha, K. Schwarz, W. Auwärter, and T. Greber, Density functional theory investigation of the geometric and spintronic structure of h-BN/Ni(111) in view of photoemission and STM experiments, Phys. Rev. B **68**, 085404 (2003).

[23] Y. Gamou, M. Terai, A. Nagashima, and C. Oshima, Atomic structural analysis of a monolayer epitaxial film of hexagonal boron nitride/Ni(111) studied by LEED intensity analysis, Sci. Rep. RITU **A44**, 211 (1997).

[24] W. Auwärter, T. J. Kreutz, T. Greber, and J. Osterwalder, XPD and STM investigation of hexagonal boron nitride on Ni(111), Surf. Sci. **429**, 229 (1999).

[25] M. Muntwiler, W. Auwärter, F. Baumberger, M. Hoesch, T. Greber, and J. Osterwalder, Determining adsorbate structures from substrate emission X-ray photoelectron diffraction, Surf. Sci. **472**, 125 (2001).

[26] R. M. Desrosiers, D. W. Greve, and A. J. Gellman, Nucleation of boron nitride thin films on Ni(100), Surf. Sci. **382**, 35 (1997).

[27] T. Greber, L. Brandenberger, M. Corso, A. Tamai, and J. Osterwalder, Single layer hexagonal boron nitride films on Ni(110), e-J. Surf. Sci. Nanotechnol. **4**, 410 (2006).

[28] M. T. Paffett, R. J. Simonson, P. Papin, and R. T. Paine, Borazine adsorption and decomposition at Pt(111) and Ru(001) surfaces, Surf. Sci. **232**, 286 (1990).

[29] M. Morscher, M. Corso, T. Greber, and J. Osterwalder, Formation of single layer h-BN on Pd(111), Surf. Sci. **600**, 3280 (2006).

[30] S. Joshi, D. Ecija, R. Koitz, M. Iannuzzi, A. P. Seitsonen, J. Hutter, H. Sachdev, S. Vijayaraghavan, F. Bischoff, K. Seufert, J. V. Barth, and W. Auwärter, Boron nitride on Cu(111): An electronically corrugated monolayer, Nano Lett. **12**, 5821 (2012).

[31] D. Usachov, A. Fedorov, O. Vilkov, V. K. Adamchuk, L. V. Yashina, L. Bondarenko, A. A. Saranin, A. Gruneis, and D. V. Vyalikh, Experimental and computational insight into the properties of the lattice-mismatched structures: Monolayers of h-BN and graphene on Ir(111), Phys. Rev. B **86**, 155151 (2012).

[32] F. Orlando, P. Lacovig, L. Omiciuolo, N. G. Apostol, R. Larciprete, A. Baraldi, and S. Lizzit, Epitaxial growth of a single-domain hexagonal boron nitride monolayer, ACS Nano **8**, 12063 (2014).

[33] G. Dong, E. B. Fourré, F. C. Tabak, and J. W. M. Frenken, How Boron Nitride Forms a Regular Nanomesh on Rh(111), Phys. Rev. Lett. **104**, 096102 (2010).

[34] T. Brugger, S. Günther, B. Wang, H. Dil, M.-L. Bocquet, J. Osterwalder, J. Wintterlin, and T. Greber, Comparison of electronic structure and template function of single-layer graphene and a hexagonal boron nitride nanomesh on Ru(0001), Phys. Rev. B **79**, 045407 (2009).

[35] N. A. Vinogradov, A. A. Zakharov, M. L. Ng, A. Mikkelsen, E. Lundgren, N. Mårtensson, and A. B. Preobrajenski, One-dimensional corrugation of the h-BN monolayer on Fe(110), Langmuir **28**, 1775 (2012).

[36] A. B. Preobrajenski, M. A. Nesterov, M. L. Ng, A. S. Vinogradov, and N. Mårtensson, Monolayer h-BN on lattice-mismatched metal surfaces: On the formation of the nanomesh, Chem. Phys. Lett. **446**, 119 (2007).

[37] A. Avsar, J. Y. Tan, X. Luo, K. H. Khoo, Y. Yeo, K. Watanabe, T. Taniguchi, S. Y. Quek, and B. Özyilmaz, van der Waals bonded Co/h-BN contacts to ultrathin black phosphorus devices, Nano Lett. **17**, 5361 (2017).

[38] S. V. Faleev, S. S. P. Parkin, and O. N. Mryasov, Brillouin zone spin filtering mechanism of enhanced tunneling magnetoresistance and correlation effects in a Co(0001)/*h*-BN/Co(0001) magnetic tunnel junction, Phys. Rev. B **92**, 235118 (2015).

[39] D. Yu. Usachov, A. V. Fedorov, O. Yu. Vilkov, A. E. Petukhov, A. G. Rybkin, A. Ernst, M. M. Otrokov, E. V. Chulkov, I. I. Ogorodnikov, M. V. Kuznetsov, L. V. Yashina, E. Yu. Kataev, A. V. Erofeevskaya, V. Yu. Voroshnin, V. K. Adamchuk, C. Laubschat, and D. V. Vyalikh, Large-scale sublattice asymmetry in pure and boron-doped graphene, Nano Lett. **16**, 4535 (2016).

[40] T. Brugger, Graphene and hexagonal boron nitride on transition metals and their application, Ph.D. thesis, University of Zürich, 2010.

[41] J. Beatty, Y. Cao, I. Tanabe, M. S. Driver, P. A. Dowben, and J. A. Kelber, Atomic layer-by-layer deposition of h-BN(0001) on cobalt: A building block for spintronics and graphene electronics, Mater. Res. Express **1**, 046410 (2014).

[42] M. S. Driver, J. D. Beatty, O. Olanipekun, K. Reid, A. Rath, P. M. Voyles, and J. A. Kelber, Atomic layer epitaxy of h-BN(0001) multilayers on Co(0001) and molecular beam epitaxy growth of graphene on h-BN(0001)/Co(0001), Langmuir **32**, 2601 (2016).

[43] J. P. Perdew, K. Burke, and M. Ernzerhof, Generalized Gradient Approximation Made Simple, Phys. Rev. Lett. **77**, 3865 (1996).

[44] K. Koepernik and H. Eschrig, Full-potential nonorthogonal local-orbital minimum-basis band-structure scheme, Phys. Rev. B **59**, 1743 (1999).

[45] M. Muntwiler, J. Zhang, R. Stania, F. Matsui, P. Oberta, U. Flechsig, L. Patthey, C. Quitmann, T. Glatzel, R. Widmer, E. Meyer, T. A. Jung, P. Aebi, R. Fasel, and T. Greber, Surface science at the PEARL beamline of the Swiss Light Source, J. Synchrotron Radiat. **24**, 354 (2017).

[46] F. J. García de Abajo, M. A. Van Hove, and C. S. Fadley, Multiple scattering of electrons in solids and molecules: A cluster-model approach, Phys. Rev. B **63**, 075404 (2001).

[47] D. P. Woodruff, Adsorbate structure determination using photoelectron diffraction: Methods and applications, Surf. Sci. Rep. **62**, 1 (2007).

[48] D. Yu. Usachov, V. Yu. Davydov, V. S. Levitskii, V. O. Shevelev, D. Marchenko, B. V. Senkovskiy, O. Yu. Vilkov, A. G. Rybkin, L. V. Yashina, E. V. Chulkov, I. Yu. Sklyadneva, R. Heid, K.-P. Bohnen, C. Laubschat, and D. V. Vyalikh, Raman spectroscopy of lattice-matched graphene on strongly interacting metal surfaces, ACS Nano **11**, 6336 (2017).

[49] M. V. Kuznetsov, I. I. Ogorodnikov, D. Yu. Usachov, C. Laubschat, D. V. Vyalikh, F. Matsui, and L. V. Yashina, Photoelectron diffraction and holography studies of 2D materials and interfaces, J. Phys. Soc. Jpn. **87**, 061005 (2018).

[50] J. B. Pendry, Reliability factors for LEED calculations, J. Phys. C **13**, 937 (1980).

[51] H. Kawanowa, H. Ozawa, T. Yazaki, Y. Gotoh, and R. Souda, Structure analysis of monolayer graphite on Ni(111) surface by Li^+-impact collision ion scattering spectroscopy, Jpn. J. Appl. Phys. **41**, 6149 (2002).